

Development and operation of a Pr₂Fe₁₄B based cryogenic permanent magnet undulator for a high spatial resolution x-ray beam line

C. Benabderrahmane,^{1,*} M. Valléau,¹ A. Ghaith,^{1,†} P. Berteaud,¹ L. Chapuis,¹ F. Marteau,¹ F. Briquez,¹ O. Marcouillé,¹ J.-L. Marlats,¹ K. Tavakoli,¹ A. Mary,¹ D. Zerbib,¹ A. Lestrade,¹ M. Louvet,¹ P. Brunelle,¹ K. Medjoubi,¹ C. Herbeaux,¹ N. Béchu,¹ P. Rommeluere,¹ A. Somogyi,¹ O. Chubar,² C. Kitegi,² and M.-E. Couprie¹

¹Synchrotron SOLEIL, L'Orme des Merisiers, Bat. A, Saint-Aubin, Gif-sur-Yvette 91192, France

²Brookhaven National Lab, PO Box 5000, Upton, New York 11973-5000, USA

(Received 12 December 2016; published 2 March 2017)

Short period, high field undulators are used to produce hard x-rays on synchrotron radiation based storage ring facilities of intermediate energy and enable short wavelength free electron laser. Cryogenic permanent magnet undulators take benefit from improved magnetic properties of RE₂Fe₁₄B (Rare Earth based magnets) at low temperatures for achieving short period, high magnetic field and high coercivity. Using Pr₂Fe₁₄B instead of Nd₂Fe₁₄B, which is generally employed for undulators, avoids the limitation caused by the spin reorientation transition phenomenon, and simplifies the cooling system by allowing the working temperature of the undulator to be directly at the liquid nitrogen one (77 K). We describe here the development of a full scale (2 m), 18 mm period Pr₂Fe₁₄B cryogenic permanent magnet undulator (U18). The design, construction and optimization, as well as magnetic measurements and shimming at low temperature are presented. The commissioning and operation of the undulator with the electron beam and spectrum measurement using the Nanoscopy beamline at SOLEIL are also reported.

DOI: 10.1103/PhysRevAccelBeams.20.033201

I. INTRODUCTION

Accelerator based x-ray sources produce nowadays very intense radiation in a broad spectral range [1,2]. Third generation synchrotron radiation light sources, with reduced emittance and large use of insertion devices provide a high brilliance with partial transverse coherence for users, enabling for example coherent imaging experiments [3]. Furthermore, fourth generation light source generally rely on the free electron laser (FEL) process using relativistic electrons propagating in a periodic magnetic field as a gain medium. FELs provide additional longitudinal coherence and extremely short pulses, enabling us to follow dynamics process of dilute species [4].

A planar undulator of period λ_u and peak field B_0 emits with an observation angle θ a radiation at wavelength λ_r and its harmonics according to:

$$\lambda_r = \frac{\lambda_u}{2\gamma^2} \left(1 + \frac{K^2}{2} + \gamma^2 \theta^2 \right) \quad (1)$$

*Also at ESRF 71 Avenue des martyrs, Grenoble 38000, France.

†amin.ghaith@synchrotron-soleil.fr

Published by the American Physical Society under the terms of the Creative Commons Attribution 4.0 International license. Further distribution of this work must maintain attribution to the author(s) and the published article's title, journal citation, and DOI.

with the deflection parameter given by $K = (eB_0\lambda_u)/(2\pi mc) = 0.0934 \times B_0[\text{T}] \times \lambda_u[\text{mm}]$, e the electron charge, m the electron mass, c the speed of light, and γ the normalized energy. The radiation produced in an undulator is very intense and concentrated in narrow energy bands in the spectrum. λ_r can be varied by a modification of the undulator magnetic field amplitude [Eq. (1)]. Undulators with high fields and short period enabling a higher number of periods to be used for a given length can be employed on intermediate energy storage rings [2] and short wavelength FEL, for providing hard x-ray radiation.

Different technologies can be used for generating the undulator periodic magnetic structure [5,6]. In the case of a permanent magnet undulator, in the so-called *Halbach* configuration [7], two parallel arrays separated by an air-gap accommodate magnets with the magnetization rotating from one block to the other by 90°. In hybrid undulators [8], the vertical magnetized magnet blocks are replaced by soft iron poles which further increase the magnetic field strength in the gap of the undulator.

The undulator peak field can be enhanced as the magnetic gap between the upper and lower arrays of magnets is decreased. The reduction of the gap is limited by the size of the vacuum chamber [9] and sets some restrictions in terms of physical aperture for the electron beam evolution. The idea to place the entire undulator in vacuum enabled the user to reach smaller gaps, and thus higher magnetic fields [10].

Rare earth materials are used for the magnets to generate the magnetic field [11]. Large coercive materials have better resistance against demagnetization that might occur due to electron beam losses or vacuum baking [12]. $\text{Sm}_2\text{Co}_{17}$ [13] magnets present a high coercivity H_{c_j} and a good radiation resistance against demagnetisation [14]. $\text{Nd}_2\text{Fe}_{14}\text{B}$ [15] magnets achieve a higher remanent field B_r , with intermediate coercivities [12]. Unfortunately large coercive $\text{Nd}_2\text{Fe}_{14}\text{B}$ magnets show small remanence magnetization. Therefore, the undulators cannot take full advantage of the magnetic performance of $\text{Nd}_2\text{Fe}_{14}\text{B}$. In order to shift further the emitted radiation toward higher energies; i.e., to the hard x-ray region, the peak magnetic field of the in-vacuum undulators can be increased when operating at cryogenic temperature. Cooling down $\text{Nd}_2\text{Fe}_{14}\text{B}$ permanent magnets increases the remanent magnetization M_r up to a certain temperature at which the process is limited by the appearance of the spin reorientation transition (SRT) phenomenon [16,17]. The easy magnetisation axis is tilted from the crystallographic c-axis [001] by an angle that increases when lowering the temperature [18]. The coercivity is not affected by the SRT phenomenon and remains increasing at low temperature. In contrast to the $\text{Nd}_2\text{Fe}_{14}\text{B}$ case, when a $\text{Pr}_2\text{Fe}_{14}\text{B}$ permanent magnet is cooled down to cryogenic temperature, no SRT occurs and its remanent magnetization keeps increasing at least until the liquid helium temperature of 4.2 K [19,20]. Such a magnet grade is well adapted for the cryogenic undulator application since it enables direct cooling at the liquid nitrogen temperature (77 K), enabling a high level of thermal stability.

Cryogenic permanent magnet undulator (CPMU) [21] is one of the evolutions of in-vacuum undulators [10]. The first prototype of 0.6 m length with a period of 14 mm, using high remanence $\text{Nd}_2\text{Fe}_{14}\text{B}$ grade cooled down to 140 K has been developed at SPring-8 [21]. Following the first demonstration at SPring-8 [21,22], several CPMU prototypes were built. After first prototypes [23,24], a 8×14.5 mm periods CPMU prototype has been built at Brookhaven National Laboratory (BNL) using $\text{Nd}_2\text{Fe}_{14}\text{B}$ grade reaching a magnetic gap of 5 mm. Another 8 periods prototype with 16.8 mm period and a gap of 5 mm hybrid undulator composed of high coercive $\text{Pr}_2\text{Fe}_{14}\text{B}$ magnets (CR-47) and Vanadium Permendur poles, have been manufactured at BNL [25] in order to investigate the resistance of the CR-47 magnets to a baking at 373 K. Helmholtz-Zentrum Berlin (HZB) with the collaboration of UCLA [26], built two CPMU prototypes (20×9 mm period and magnetic gap of 2.5 mm), using $\text{Pr}_2\text{Fe}_{14}\text{B}$ magnets cooled down to 20–30 K. At SOLEIL, three hybrid prototypes CPMU have been built and characterized: A 4 periods 18 mm length with $\text{Nd}_2\text{Fe}_{14}\text{B}$ magnets (BH50 Hitachi-Neomax) [27], a 4×18 mm period with $\text{Pr}_2\text{Fe}_{14}\text{B}$ (CR53 Hitachi-Neomax) [28], and a 4×15 mm period with $\text{Pr}_2\text{Fe}_{14}\text{B}$.

The first full scale cryogenic undulator had been developed at European Synchrotron Radiation Facility (ESRF) [29] with a period length of 18 mm using a relatively low remanence $\text{Nd}_2\text{Fe}_{14}\text{B}$ magnet grade ($B_r = 1.16$ T) cooled down to around 150 K, reaching a gap of 6 mm. ESRF recently developed two more cryogenic undulators, one with the same period length as the first using a high remanence $\text{Nd}_2\text{Fe}_{14}\text{B}$ ($B_r = 1.38$ T) cooled down to 135 K [30], and a second one of period 14.5 mm using $\text{Pr}_2\text{Fe}_{14}\text{B}$ magnet grade cooled down to 100 K. Based on the ESRF development, Danfysik build for Diamond [31] a 17.7 mm period cryogenic undulator using high remanence $\text{Nd}_2\text{Fe}_{14}\text{B}$ magnets cooled down to 150 K and a magnetic gap of 5 mm. $\text{Pr}_2\text{Fe}_{14}\text{B}$ based CMPUs are under construction at Diamond. SPring-8 in collaboration with SLS [32] developed a cryogenic undulator using high remanence $\text{Nd}_2\text{Fe}_{14}\text{B}$ cooled down around 140 K. The cryogenic undulators developed so far use $\text{Nd}_2\text{Fe}_{14}\text{B}$ permanent magnet working around 140 K. They are cooled down to the liquid nitrogen temperature at 77 K and heated to reach the working temperature in order to avoid the SRT phenomenon appearance. HZB is currently building 2 new $\text{Pr}_2\text{Fe}_{14}\text{B}$ based CPMU (1.6 m long with a 17 mm period with a gap of 5 mm, and a 2 m long with 15 mm period and a gap of 2 mm). A 2 m long cryogenic undulator with 140×13.5 mm period is under construction for the High Energy Photon Source Test Facility (HEPS-TF) in Korea. $\text{Pr}_2\text{Fe}_{14}\text{B}$ based CMPUs are under construction at National Synchrotron Radiation Research Center [33].

In this paper, the development of the first full scale (2 m long) $\text{Pr}_2\text{Fe}_{14}\text{B}$ cryogenic undulator which has been installed on a storage ring is presented, i.e., SOLEIL in France. It has 107 periods of length 18 mm. The magnetic analysis and measurement results indicate that the quality of the magnet grade satisfies the undulator requirements and demonstrate a further increase of magnetic field (by a few percents). We show that the direct operation at 77 K enables a good thermal stability. We also present the design, construction steps (with optimization, magnetic measurements and shimming at low temperature). We then report on the commissioning with the electron beam and the current successful operation both from an electron or photon point of view (with measurements of undulator radiation). Indeed, we show some results of photon beam alignment using the Nanoscopium long section beam line, or precise adjustment of the undulator taper with the photon beam itself.

II. DESIGN OF THE CRYOGENIC UNDULATOR

A. Magnetic design

The SOLEIL $\text{Pr}_2\text{Fe}_{14}\text{B}$ based U18 cryogenic undulator has been modeled using RADIA [34] software, as illustrated in Fig. 1. The characteristics are indicated in Table I, considering the longitudinal coordinate s , the transverse

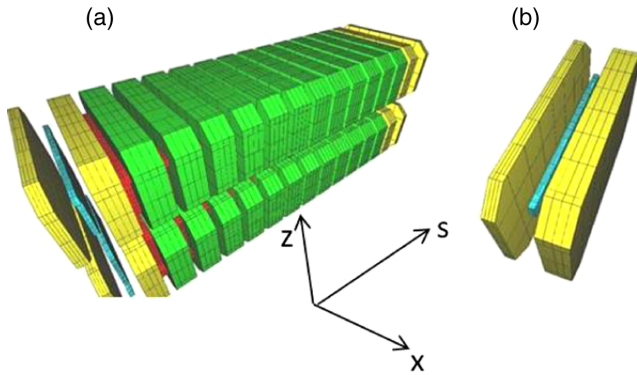


FIG. 1. Magnetic design using RADIA [34]. (a) Seven period undulator: permanent magnet (green) of the main undulator part ($50 \times 30 \times 6.5 \text{ mm}^3$), Poles of the main undulator part (red) ($33 \times 22 \times 2.5 \text{ mm}^3$), permanent magnet (yellow) of the extremity part of the undulator (80% and 35% of the main magnet width) [35]. Pole of the extremity part (blue) of the undulator (50% of the main polewidth). (b) Extremity part of the magnetic design.

horizontal and vertical are x and z respectively. The model contains two parts; the central one [Fig. 1(a)] constituted by full size permanent magnets and poles producing the main magnetic field of the undulator, and the extremities [Fig. 1(b)] located at each end of the undulator constituted by two magnets and one pole. The extremity parts are optimized to minimize the on-axis field integral variations versus the undulator gap [35].

For a given deflection parameter and total undulator length, the increase of the undulator magnetic field allows for the reduction of the period, so the number of periods could be enhanced, resulting in higher flux and brilliance. Figure 2 presents the on-axis magnetic peak field versus gap calculated for cryogenic undulators U18 ($\text{Pr}_2\text{Fe}_{14}\text{B}$), U20 ($\text{Nd}_2\text{Fe}_{14}\text{B}$, and $\text{Sm}_2\text{Co}_{17}$). The magnetic field of U18

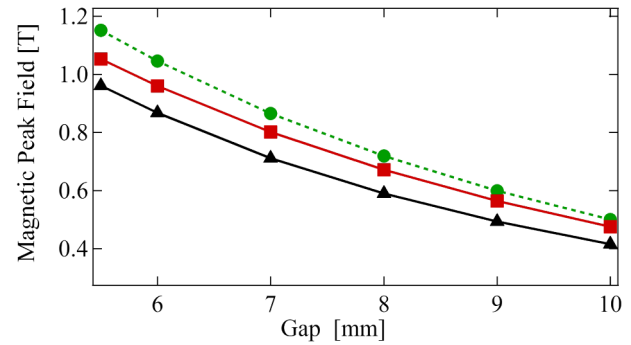


FIG. 2. On-axis magnetic peak field calculated with RADIA. (Filled circle) U18 $\text{Pr}_2\text{Fe}_{14}\text{B}$ cryogenic undulator at 77 K, $B_r = 1.57 \text{ T}$ at 77 K, magnet dimensions $50 \text{ mm} \times 30 \text{ mm} \times 6.5 \text{ mm}$, pole dimensions $33 \text{ mm} \times 22 \text{ mm} \times 2.5 \text{ mm}$. (Filled square) U20 $\text{Nd}_2\text{Fe}_{14}\text{B}$ in-vacuum undulator at 293 K, $B_r = 1.25 \text{ T}$ at 293 K, magnet dimensions $50 \text{ mm} \times 30 \text{ mm} \times 7.5 \text{ mm}$, pole dimensions $33 \text{ mm} \times 22 \text{ mm} \times 2.5 \text{ mm}$. (Filled triangle) U20 $\text{Sm}_2\text{Co}_{17}$ in-vacuum undulator at 293 K, $B_r = 1.05 \text{ T}$ at 293 K, magnet dimensions $50 \text{ mm} \times 30 \text{ mm} \times 7.5 \text{ mm}$, pole dimensions $33 \text{ mm} \times 22 \text{ mm} \times 2.5 \text{ mm}$.

cryogenic undulator cooled down to 77 K is $\sim 10\%$ higher than U20 $\text{Nd}_2\text{Fe}_{14}\text{B}$ based undulator and $\sim 20\%$ higher than U20 $\text{Sm}_2\text{Co}_{17}$ at room temperature.

B. Expected spectral properties

In the case of SOLEIL, the 18 mm period is chosen to keep the deflection parameter K close to the value used for U20 in-vacuum undulators. The number of periods to be assembled can be increased by 11% with the same undulator length, which enhances the brightness for the same photon energy spectrum range.

The spectral performance of the $\text{Pr}_2\text{Fe}_{14}\text{B}$ cryogenic undulator U18 is compared to the in-vacuum undulator U20 $\text{Nd}_2\text{Fe}_{14}\text{B}$ and U20 $\text{Sm}_2\text{Co}_{17}$ used in SOLEIL storage ring on a long straight section (see Table II for the parameters). The period is slightly adjusted so that typically the same spectral range is covered and the total length is kept constant. Figure 3 and Fig. 4 respectively show the brilliance and spectral flux calculated with SRW software [36] for the three given undulators mentioned before. Larger brilliance and flux is achieved with U18 than the two U20 undulators. At a photon energy of 30 keV, U18

TABLE I. SOLEIL Cryogenic undulator main characteristics.

Item	Unit	Value
Technology		Hybrid
Magnet Material CR53 (Hitachi)		$\text{Pr}_2\text{Fe}_{14}\text{B}$
Remanence B_r	T	1.35 at 293 K 1.57 at 77 K
Coercivity H_{cj}	T	1.63 at 293 K 7.6 at 77 K
Magnet size (x, z, s)	mm^3	$50 \times 30 \times 6.5$
Pole material		Vanadium Permandur
Pole size (x, z, s)	mm^3	$33 \times 22 \times 2.5$
Period	mm	18
Minimum magnetic gap	mm	5.5
Maximum magnetic gap	mm	30
Magnetic peak field at minimum gap	T	1.152
Deflection parameter		1.936
Number of periods		107

TABLE II. Characteristics of the electron beam in SOLEIL long section beam line.

Parameters	Value	Unit
Energy	2.75	GeV
Current	0.5	A
Emittance H	3.9	nm rad
Emittance V	0.039	nm rad
RMS energy spread	0.1016	%

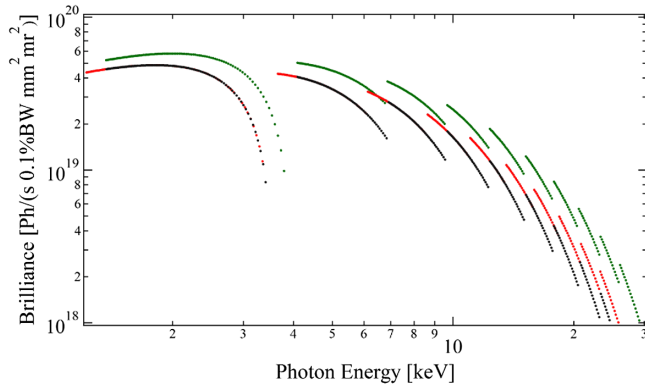


FIG. 3. Brilliance in logarithmic scale with gap = 5.5 mm calculated with SRW [36] for three different undulators: (Black) U20 $\text{Sm}_2\text{Co}_{17}$ (100 periods) with peak field of 0.971 T, (Red) $\text{Nd}_2\text{Fe}_{14}\text{B}$ (100 periods) with peak field of 1.053 T, and (Green) $\text{Pr}_2\text{Fe}_{14}\text{B}$ (110 periods) with peak field of 1.152 T at cryogenic temperature. Electron beam characteristics of Table II, with $\beta_x = 5.577$ m, $\beta_z = 8.034$ m, $\alpha_x = 0$, $\alpha_z = 0.001$ rad), through a window aperture of 0.1 mm \times 0.1 mm placed at a distance of 11.7 m.

flux is ~ 2 times higher than the one of the U20 $\text{Nd}_2\text{Fe}_{14}\text{B}$ undulator and 2.5 times higher than U20 $\text{Sm}_2\text{Co}_{17}$ undulator.

In the case of cryogenic undulators, these energies are obtained at lower harmonic order than in the case of room temperature in-vacuum undulators. In consequence, there is less intensity reduction due to the undulator imperfections, since lower order harmonics are less sensitive to phase error σ_ϕ [37,38]. Indeed, phase error is due to the magnetic field errors along the undulator axis, such as variations in the peak field or the period length from one period to another. It causes change in the length of the electron trajectory and yields a phase lag Φ , between the electron and the photon

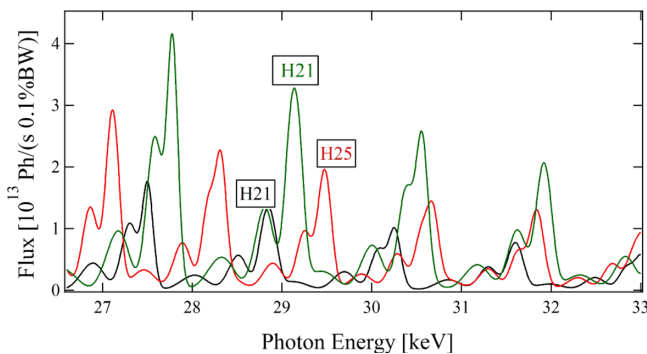


FIG. 4. Spectra calculated (using SRW) with beam and undulator parameters of Fig. 3. (Green) U18 $\text{Pr}_2\text{Fe}_{14}\text{B}$ cryogenic undulator at 77 K, with $K = 1.937$. (Red) U20 $\text{Nd}_2\text{Fe}_{14}\text{B}$ in-vacuum undulator at 293 K with $K = 1.967$. (Black) U20 $\text{Sm}_2\text{Co}_{17}$ in-vacuum undulator at 293 K $K = 1.812$. H with the index represents the harmonic number at photon energy ~ 29 keV.

expressed as: $\Phi = \frac{2\pi}{\lambda_R} \left(\frac{l(s)}{\beta} - s \right)$ where $l(s)$ is the path traveled by the electron up to the point s . In the case of an undulator with phase error, the phase lag which is no longer zero causes photon interference to occur on different wavelengths as well as destructive interference, which results in line broadening and intensity reduction of the emitted lines. The effect is larger on higher harmonics, due to the fact that they are more sensitive to the phase slippage. Indeed, the intensity reduction can be expressed as: $I_n = I_{n0} \exp(-n^2 \sigma_\phi^2)$ with n the harmonic order, and I_{n0} the intensity without phase error. For example, 29 keV is reached on harmonic 21 with the cryogenic U18 $\text{Pr}_2\text{Fe}_{14}\text{B}$ and harmonic 25 with U20 $\text{Nd}_2\text{Fe}_{14}\text{B}$ as shown in Fig. 4. For a 2.5° phase error, the intensity reduction of the 21 harmonic is calculated to be of factor ~ 0.56 , as for the 25 harmonic the reduction is of the factor ~ 0.70 . However the effect of phase errors can become less severe than predicted by the above equation when electron beam emittance and energy spread are taken into account. So with low phase error, higher harmonics with a fair intensity can be achieved.

C. Mechanical design

Figure 5 presents the mechanical design of the cryogenic undulator U18 inspired from the in-vacuum undulator [39]. The carriage is constituted of a metallic base where the frame is welded. Two out-vacuum (external) girders are fixed on the frame and can move vertically thanks to two series of sliders. The magnetic systems (permanent magnets, poles and their mechanical supports) are fixed on two in-vacuum girders connected to the external ones by 24 rods. The in-vacuum girders are separated by a gap where

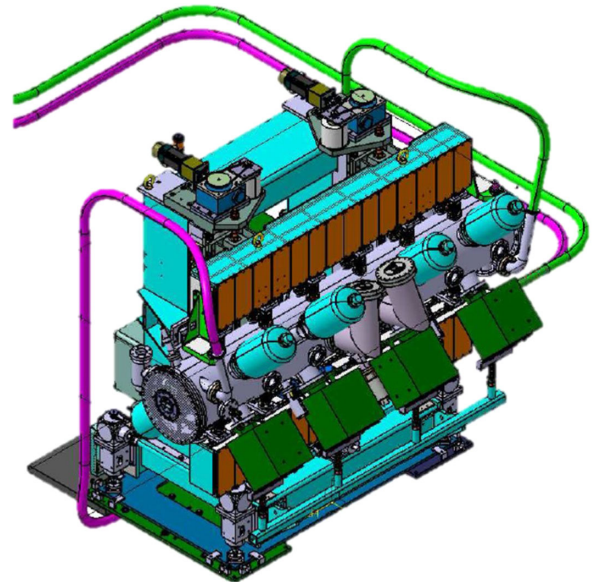


FIG. 5. Mechanical design of the cryogenic undulator using 3D CATIA (<http://www.3ds.com/fr/>).

the electron beam crosses the undulator. The gap variation (from minimum value of 5.5 mm to maximum value of 30 mm) is enabled by two steps motors Berger Lahr VRDM3910; a third step motor is used to move vertically the undulator over a 10 mm range in order to align in the vertical direction the magnetic axis with the electron beam axis. The in-vacuum girders with the magnetic system are installed in a vacuum chamber equipped with Ion pumps, Titanium sublimation pumps and instrumentation to ensure an ultra high vacuum in the vacuum chamber during the operation with electron beam. Cu-OFHC tapers are fixed on the vacuum chamber and on the in-vacuum girders to guarantee a smooth variation of the impedance seen by the electron beam when it crosses the undulator.

A copper absorber is installed at the downstream of the undulator inside the vacuum chamber to collect the undesired photon beam coming from the upstream bending magnet. The absorber is cooled down with water at room temperature. A 100 μm Cu-Ni foil is placed on the magnetic system and stretched at the extremities of the undulator by a spring tensioner system. It conducts the image current generated by the electron beam when it crosses the undulator at a very close position from the magnetic system. Permanent magnets and different parts of the undulator inside the vacuum chamber are equipped with 55 temperature sensors (thermocouples and platinum sensors PT100), which are fixed on the girders, LN2 tubes, modules holders, and directly on magnets, in order to measure the temperature during the cooling down and storage ring operation.

The main difference between the cryogenic undulator and a room temperature in-vacuum undulator is the cooling system. In the cryogenic undulator using $\text{Nd}_2\text{Fe}_{14}\text{B}$, the in-vacuum girders are connected to the cooling pipes (cooled down to the liquid nitrogen temperature of 77 K) through longitudinally distributed spacers acting as thermal resistors to bring the magnetic system temperature to around 150 K [29–32]. In contrast with $\text{Nd}_2\text{Fe}_{14}\text{B}$ based cryogenic undulators, $\text{Pr}_2\text{Fe}_{14}\text{B}$ based cryogenic undulators are cooled down directly to 77 K, in which the liquid nitrogen crosses the in-vacuum girders (Aluminum with a thermal conductivity of 237 W/Km and a thermal expansion coefficient of 23.6×10^{-6} K/m) through a 12 mm diameter hole, where its inner surface is cooled directly by liquid nitrogen, guaranteeing a better temperature distribution and thus a smaller thermal gradient along the magnetic system.

Table III presents the total calculated thermal heat load dissipated by the liquid nitrogen closed loop in the case of the U18 build at SOLEIL. The heat load comes from heat deposited by the beam (wakefield and synchrotron radiation), the vacuum chamber, and the rods. The heat load coming from the electron beam represents more than 22% of the total heat load, due to the synchrotron radiation coming from the upstream dipole and the wake field power deposited by the passage of the electron beam on the liners

TABLE III. Total heat load dissipated by the liquid nitrogen close loop.

Heat load source	Power (W)
Vacuum Chamber	70
Rods	104
Electron beam	50
Total power dissipated	224

and tapers. Half of the dissipated heat load is coming from the rods, which connect the out-vacuum and in-vacuum girders. The diameters and contact surfaces of the rods have been reduced without any effect on their rigidity to reduce the heat load. Since the vacuum chamber is at room temperature, whereas the in-vacuum girders are at liquid nitrogen temperature, the inside part of the vacuum chamber has been polished to improve the emissivity and to reduce the heat load by a factor of 2.

The cooling down of the undulator to liquid nitrogen temperature causes contraction on the in-vacuum girders and the rods. The longitudinal contraction of the in-vacuum girder by 8 mm is then taken into account in the magnet assembly at room temperature by keeping 40 μm between magnet modules. The transverse contraction of each rod by ~ 0.5 mm causes an opening of the gap by 1 mm, which should be adjusted before conducting magnetic measurements.

III. ASSEMBLY, MAGNETIC OPTIMIZATION AND MEASUREMENT OF THE CRYOGENIC UNDULATOR

A. Assembly and optimization at room temperature

The assembly and the magnetic corrections of the cryogenic undulator are performed at room temperature in the same conditions as a standard in-vacuum undulator. A standard magnetic bench allowing Hall probe and flip coil measurements has been used for the assembly and corrections at room temperature. An optimization software called ID-Builder [40] developed at SOLEIL has been used at all steps of the undulator construction: magnets sorting, period assembly, shimming (vertical displacement of magnets and poles to correct the field integrals and the phase error), and magic fingers (small magnets installed at the extremities of the undulator to correct the field integral). The electron beam should emit the most intense radiation when it crosses the undulator without disturbing the beam dynamics in the storage ring. The figures of merit during the assembly and corrections are the field integrals, the trajectory straightness and the phase error. They have to be minimized to reduce the impact of the magnetic errors on the undulator performances in terms of photon spectrum and beam dynamics.

Figure 6 presents the vertical field integral I_z and the horizontal field integral I_x of the cryogenic undulator

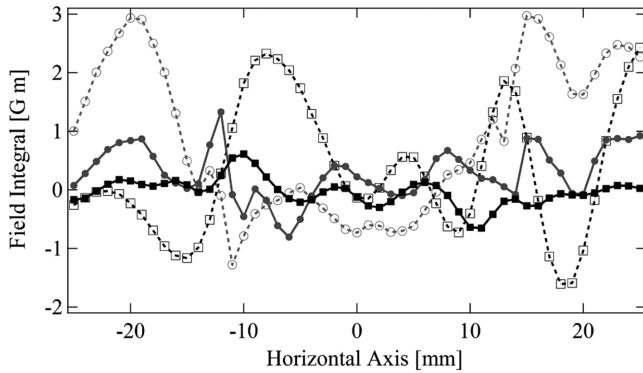


FIG. 6. Field integrals versus horizontal position at minimum gap of 5.5 mm at room temperature. (Filled square) Vertical field integral (I_z) after magic finger corrections. (Filled circle) Horizontal field integral (I_x) after magic finger corrections. (Open square) Vertical field integral (I_z) before magic finger corrections. (Open circle) Horizontal field integral (I_x) before magic finger corrections. Field integrals precision is ~ 0.05 G m.

versus transverse position at minimum gap of 5.5 mm at the end of the assembly at room temperature and after the complete iterative correction process. After the corrections, the undulator field integrals present a smoother variation versus horizontal position and the on-axis integral is less than 0.4 G m and the higher off-axis field integral are reduced from 3 G m to less than 1 G m.

Figure 7 presents the electron beam trajectory in the cryogenic undulator calculated from the magnetic field measurements versus the longitudinal position at the end of the assembly at room temperature and after the corrections. The trajectory position at the exit of the undulator after the magnetic assembly is $8 \mu\text{m}$, it is kept below $2 \mu\text{m}$ after magnetic corrections.

The RMS phase error (calculated by B2E from the measured magnetic field [41]) at minimum gap after the magnetic assembly of the undulator is found to be 14.5° ,

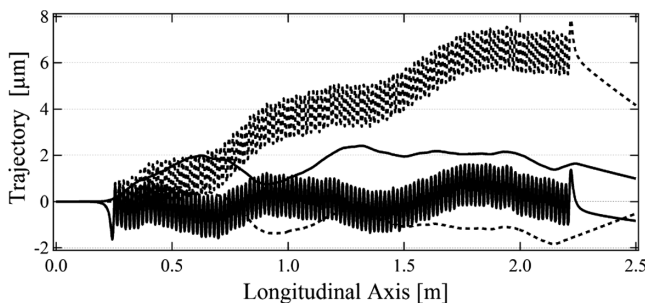


FIG. 7. Electron beam trajectory in the cryogenic undulator at room temperature calculated with B2E code from Hall probe magnetic measurement at SOLEIL ($E = 2.75$ GeV), with a precision of 0.5 Gauss. (Solid line) Horizontal and vertical trajectories after the assembly and corrections. (Dashed line) Horizontal and vertical trajectories after the assembly and before shimming.

and has been corrected to 2.8° after shimming the magnet modules. The vertical position of the magnet modules is modified by using shims (copper pieces) to correct locally the magnetic field value.

B. Cryogenic magnetic measurement bench

Magnetic measurement benches have been developed over the past years to increase precision and enable to conduct measurements for insertion devices at low temperature. A cryogenic undulator requires a specific bench with certain characteristics. ESRF [30] had developed a magnetic bench to perform magnetic field measurements for cryogenic undulators. This bench is mounted inside a vacuum chamber, where the Hall probe (with a ball bearing) is fixed on a mobile carriage guided along a rail. The longitudinal position of the Hall probe is measured with a laser tracker. The stretched wire motion is performed by two translation motors located outside the vacuum chamber and transmitted inside by rods through bellows. SPring-8 developed a bench called SAFALI [42] for Hall probe magnetic measurements and is mounted inside the vacuum chamber of the undulator. The Hall probe is displaced longitudinally by a vacuum compatible stepper motor installed inside the vacuum chamber. The mechanical default position of the Hall probe on the rail is measured with lasers and corrected with small displacements on the rail. Helmholtz-Zentrum Berlin (HZB) built a 2 m long in-vacuum Hall-probe measuring bench [43] for the characterization of several in-vacuum cryogenic undulators under development. The bench employs a system of laser interferometers and position sensitive detectors, which are used in a feedback loop for the Hall probe position and orientation.

Figure 8 presents the cryogenic magnetic measurement bench developed at SOLEIL. It is used to measure the field created by the undulator at both room and cryogenic temperature. The local magnetic field and field integrals

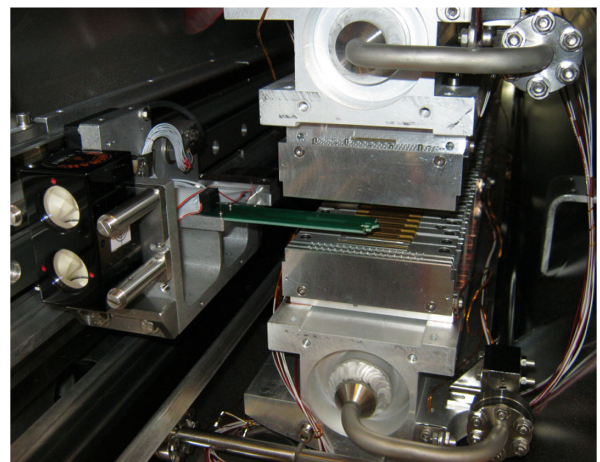


FIG. 8. SOLEIL dedicated magnetic measurement bench inside the vacuum chamber of the cryogenic undulator.

are measured by a Hall probe (model Bell GH701) and a stretched wire, respectively. The cryogenic magnetic measurement bench is installed inside the undulator vacuum chamber and is removed after the measurements. The Hall probe is fixed on a trolley which moves on a rail by a stepper motor, mounted outside the vacuum chamber and whose movement is transmitted inside the vacuum chamber via a magnetic coupling system. The rail is mechanically independent of the vacuum chamber and is fixed from the outside by seven rods. The deformations of the rail are measured with an optical system and the longitudinal position of the Hall probe is measured with a thermalized optical rule (Heidenhain LIDA 405). The deformations of the rail are measured with an optical system constituted by an angular reflector for the Hall probe angular deformation measurements, and a linear reflector (Renishaw) for the Hall probe horizontal and vertical deformation measurements.

The cryogenic magnetic bench is aligned inside the vacuum chamber. The angular deformations of the bench are corrected by using shims with different thicknesses installed at the deformation location, however the vertical deformation of the bench is not corrected mechanically by shims, and it is corrected directly on the magnetic measurement results.

Figure 9 presents the rotation angle of the Hall probe at different longitudinal positions before and after correction. Indeed, the field measured by the Hall probe depends on its position according to Eq. (2).

$$B_c(s) = B_0(s) \cdot f \cdot \cosh^{-1} \left(\frac{2\pi d_z}{\lambda_u} \right) \quad (2)$$

where B_c is the corrected magnetic field, B_0 the measured magnetic field, d_z the vertical default position, s the longitudinal position and f is a factor which depends on the undulator characteristics, a RADIA calculation

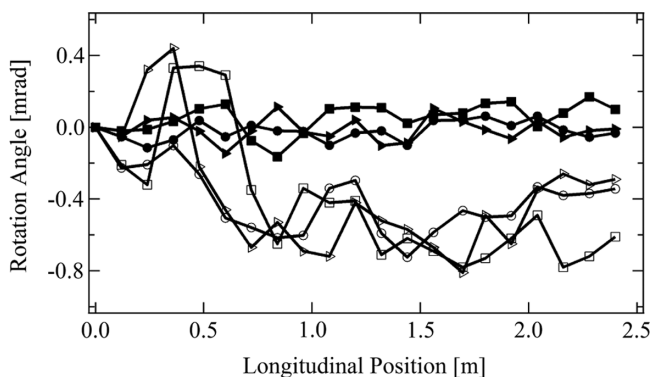


FIG. 9. Hall probe rotation angle versus longitudinal position. (Filled circle) θ_x after corrections, (filled square) θ_z after corrections, (filled right triangle) θ_x after corrections, (open circle) θ_s before corrections, (open square) θ_z before corrections (open right triangle) θ_x before corrections.

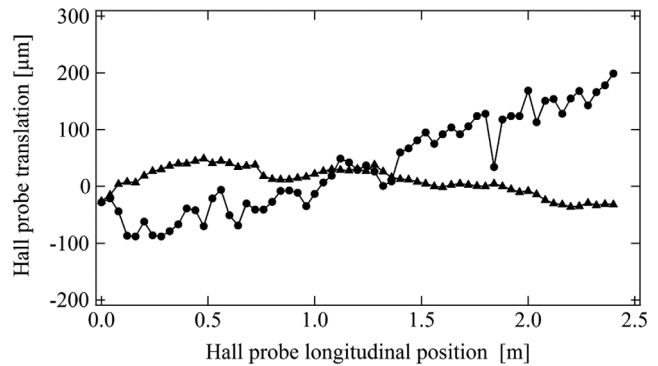


FIG. 10. Hall probe translation versus longitudinal position. (Filled circle) Translation in the vertical z axis direction, (triangle) translation in the horizontal x axis direction.

identifies a value of $f = 0.816$ that is valid for gaps between 5 mm and 10 mm.

The angle of the Hall probe of 0.8 mrad measured with a laser interferometer has been reduced down to 0.1 mrad by inserting small mechanical shims along the longitudinal position. The original angle measured at 20 cm would provide an error of 160 μm on axis, which corresponds to an equivalent field variation of 22 Gauss. Whereas after correction, it provides an error of 20 μm on axis and a remaining field variation of 0.35 Gauss.

Figure 10 presents the measured horizontal and vertical Hall probe position defects of the cryogenic magnetic bench. The horizontal Hall probe position variation is 81 μm along the bench, which corresponds to a field change calculated with RADIA of 6.5 Gauss (or a relative change of 0.06%). However, the vertical variation of 287 μm along the bench corresponds to a field variation calculated with RADIA of 129 Gauss (or a relative change of 1.1%). Such a change is significant and is corrected for the magnetic field measurement using Eq. (2).

Since a temperature variation could occur from the Hall probe displacement from the entry to the exit of the undulator, the Hall probe has been calibrated prior with temperature variation on purpose. The resistance of the Hall probe (R) is measured at different temperatures (T). A linear variation with temperature is measured, given by $R(T) = a + bT$ with $a = -56.36 \pm 0.379 \Omega$, $b = 0.192 \pm 0.002 \Omega/\text{K}$. Indeed, the Hall probe temperature was changed by 4 K during the magnetic measurements from entry to exit of the undulator. This variation and the thermal sensitivity coefficient of the Hall probe $-0.0043\%/K$ (at $T = 293 \text{ K}$) have been taken into account to correct the measured magnetic field values.

C. Cooling at cryogenic temperature

Figure 11 presents the magnet temperature and vacuum pressure variation during the cooling down of the cryogenic undulator using a cryocooler system (Cryotherm Bruker). The magnets reach liquid nitrogen temperature of 77 K

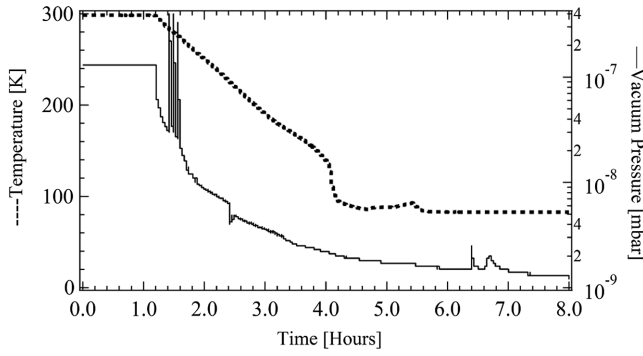


FIG. 11. Cooling down of the cryogenic undulator. (Normal line) Undulator vacuum pressure, (dashed line) permanent magnets temperature.

after 6 hours. The undulator is not baked in order to avoid demagnetization due to low coercivity for the selected magnet grade. However the undulator vacuum pressure drops quite rapidly due to the cold mass which acts as a cryo-pump.

D. Warming up

The warming of the undulator from cryogenic to room temperature is relatively long, about 72 hours, but it could be accelerated (if needed) by injecting nitrogen gas at 60 °C in the cooling circuit. Figure 12 shows the warming of the undulator by injecting nitrogen gas ($T = 60^\circ\text{C}$) under 2.5 bar in the undulator to reduce again this long delay to approximately 24 hours.

E. Measurements and magnetic measurements at cryogenic temperature

Figure 13 presents the electron trajectory at room temperature and cryogenic temperature calculated from the measured magnetic field. Despite the cooling down, the electrons trajectory position is kept below $4 \mu\text{m}$ along the undulator.

The cryogenic undulator RMS phase error has been corrected (using shims) at room temperature to 2.8° . After

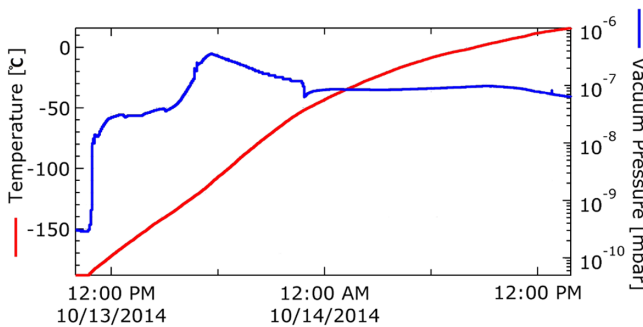


FIG. 12. Warming up the undulator to room temperature. (Blue) Undulator vacuum pressure, (Red) permanent magnets temperature.

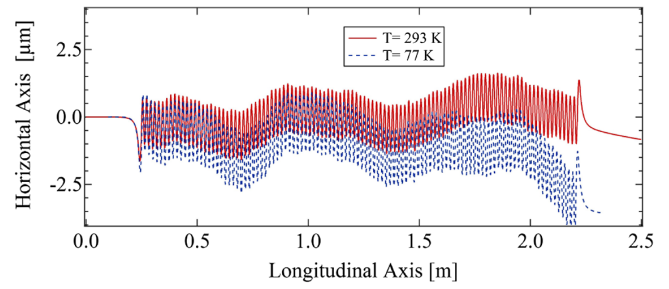


FIG. 13. Electron beam trajectory calculated from the measured magnetic field. (Line) At room temperature 293 K, (dashed) at cryogenic temperature 77 K after rod length correction.

the cooling down, the RMS phase error is increased to 9.1° because of mechanical contractions. The rods are contracted vertically by 1 mm, the variation of this contraction between rods causes in-vacuum girder deformation and then phase error degradation. Mechanical shims have been used to modify the vertical position of the 24 rods in order to correct the RMS phase error and bring it down to 3° . The thickness of the shim is calculated using Eq. (3).

$$\Delta B = B_0 \left[\exp \left(-\frac{\pi \Delta_g}{\lambda_u} \right) - 1 \right] \quad (3)$$

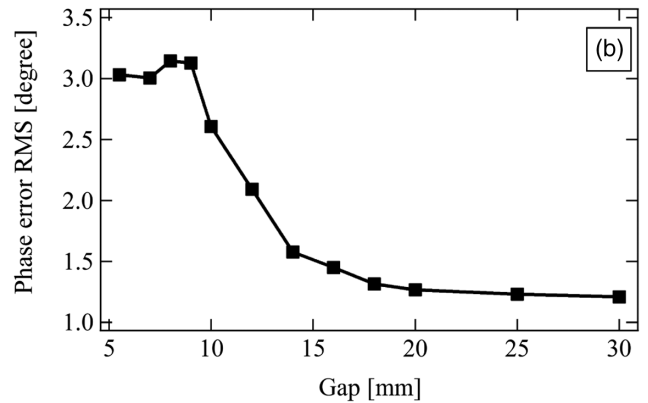
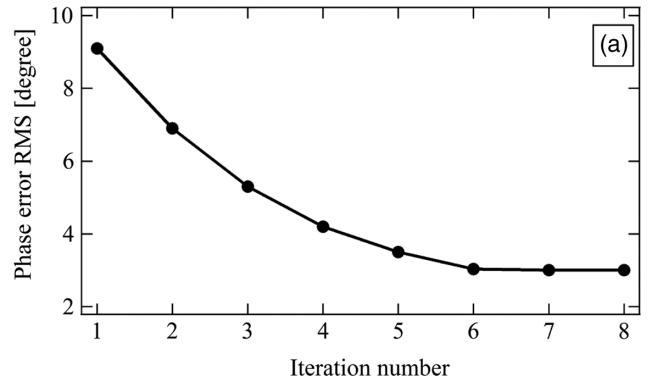


FIG. 14. (a) Phase error corrections with rod vertical displacement at minimum gap of 5.5 mm. (b) Phase error variation versus gap after correction.

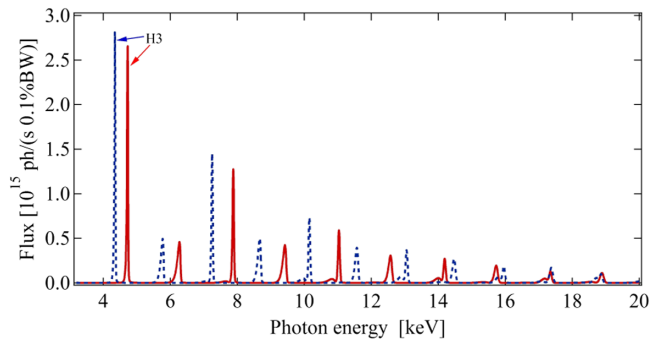


FIG. 15. U18 spectrum calculated with SRW code at a distance of 17 m from the source point through a slit of 0.1 mm \times 0.1 mm at minimum gap of 5.5 mm. (Solid line) At room temperature of 293 K, (dashed line) at cryogenic temperature of 77 K. Beam characteristics shown in Table II.

where ΔB is the magnetic field variation after a gap variation of Δg , and B_0 is the measured magnetic field before the gap modification.

And for a small Δg , Eq. (3) can be written as:

$$\frac{\Delta B}{B_0} = -\frac{\pi \Delta g}{\lambda_u} \quad (4)$$

Figure 14(a) presents the improvement of the phase error calculated from the magnetic field measurement at 77 K during rods shimming iterations. The 3° RMS phase error is obtained from the 6th iteration; the 7th and 8th iterations do not improve further the phase error.

Figure 14(b) presents the phase error variation after rod length correction versus gap. The value at minimum gap of 5.5 mm is 3° RMS, the maximum value is a 3.2° RMS at gap 8 mm.

Figure 15 presents the spectrum of the cryogenic undulator at room temperature and cryogenic temperature of 77 K calculated from the measured magnetic field at minimum gap. At 77 K the photon flux increases by 24% for the seventh harmonic and 34% for the ninth harmonic.

IV. OPERATION OF THE CRYOGENIC SYSTEM ON THE SOLEIL STORAGE RING

A. Commissioning with the electron beam

Figure 16 presents the cryogenic undulator installed in the long straight section SDL13 in SOLEIL storage ring. This straight section has been modified to allow for the installation of two canted in-vacuum undulators in order to extract two different long beam lines NANOSCOPIUM and ANATOMIX [44].

1. Alignment of the undulator with the electron beam

After the installation and alignment of the undulator in the tunnel, the magnetic axis has to match with the electron beam path in the straight section. A vertical misalignment

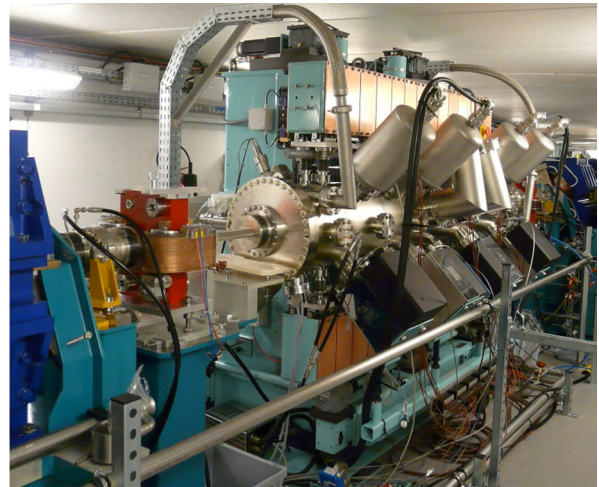


FIG. 16. The cryogenic undulator installed in the SOLEIL storage ring straight section.

of the undulator has a very strong effect on the magnetic field and leads to a nonoptimized phase error and trajectories. To perform this optimization with the electron beam, the whole carriage is moved in the vertical direction (offset movement) between ± 2 mm at a fixed gap of 5.5 mm and for each offset value, the vertical tune values are recorded (see Fig. 17). The magnetic axis corresponds to the offset value, where the magnetic field, and hence the vertical tune, are minimum. The reproducibility of this measurement is 50 μ m.

The magnetic axis can also be determined by measuring the decay of the electron beam current versus offset.

2. Vacuum and thermal evolutions

Figure 18 presents the evolution of the undulator vacuum pressure during the first closing of the gap at high beam current of 400 mA. The gap has been closed in only 40 min and the maximum pressure reached 3×10^{-8} mbar.

Figure 19 displays the evolution of the undulator permanent magnet temperature during the first closing at the minimum gap at high beam current of 400 mA. The

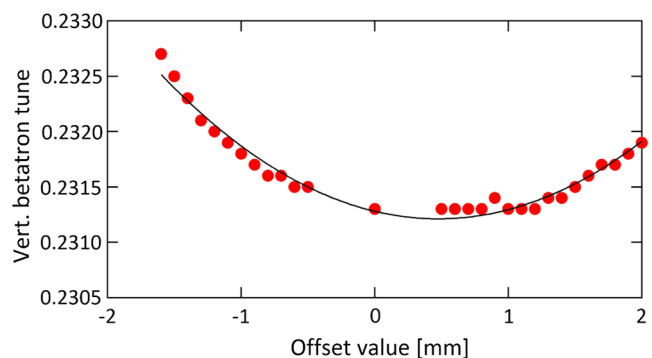


FIG. 17. Vertical betatron tune versus offset: (filled circle): experimental vertical tune measurement, (line): fitting curve.

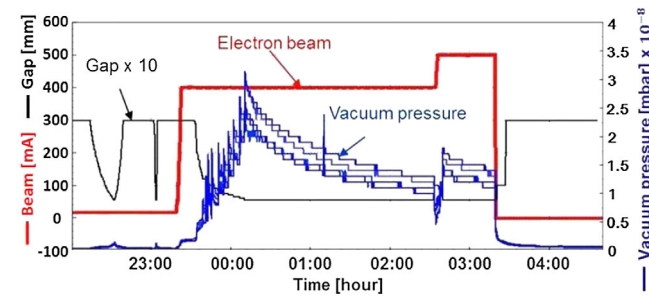


FIG. 18. Undulator vacuum pressure variation versus gap at high electron beam current of 400 mA.

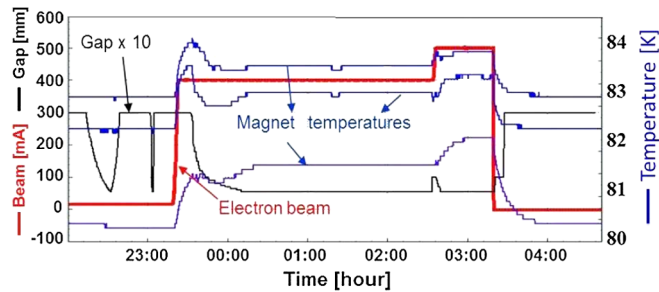


FIG. 19. Permanent magnet temperature variation versus gap at high electron beam current of 400 mA.

average permanent magnet temperature without the electron beam is found to be 82 ± 1.8 K. It increases only by 2 K at high electron beam of 400 mA. The temperature variation determined by the sensors installed along the undulator is caused by the contact of these sensors with the magnets, and hence the variation is not linear along the longitudinal position.

B. Effects on the electron beam

The focusing effect of the cryogenic undulator on the electron beam has been measured as a function of gap. Focusing effects are inherent to the ideal magnetic field configuration (B_0^2 scaling of the dynamic integrals) and to magnetic field errors (normal integrated gradient measured on the magnetic bench). Figure 20 presents the variation of both horizontal and vertical tunes versus gap. As expected from magnetic measurements, a significant horizontal focusing is observed due to the nonzero normal integrated gradient measured on the bench (+200 G). Actually the magnetic correction strategy was to perfectly cancel the skew integrated gradient term to the detriment of the normal one. The vertical focusing is then reduced compared to the one expected from the measured vertical field scaling.

C. Spectral performance on the beam line

The U18 cryogenic undulator is in use by the NANOSCOPIUM long beam line. This 155 m long

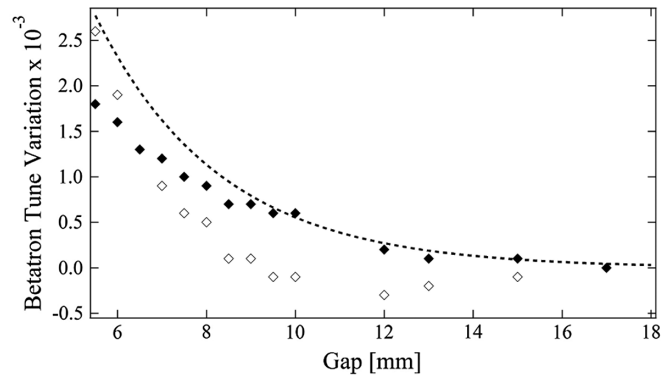


FIG. 20. Variation of the measured horizontal (white diamonds) and vertical (black diamonds) tune variation as a function of gap. The vertical tune variation is compared to the expected one from measured vertical field scaling (dashed line).

multimodal beam line [45,46] is dedicated to scanning hard x-ray nano-probe experiments in the 30 nm – 1 μ m spatial resolution range by combining x-ray fluorescence (XRF), absorption spectroscopy (XAS), and phase-contrast imaging). NANOSCOPIUM aims at reaching 30–200 nm resolution in the 5–20 keV energy range for routine user experiments. The beam line design tackles the tight stability requirements of such a scanning nano-probe by creating an overfilled secondary source, implementing all horizontally reflecting main beam line optics, and constructing a dedicated high stability building envelope. This beam line provides high sensitivity elemental and sample morphology mapping with down to 30 nm spatial resolution by fast scanning spectro-microscopy combined with absorption, differential phase contrast and dark field imaging and electron density mapping by coherent imaging techniques. The typical scientific fields cover biology and life sciences, earth- and environmental sciences, geo-biology and bio-nanotechnology. The beam line is especially well suited for studies seeking information about highly heterogeneous systems at multiple length scales also in natural or in operando conditions.

1. Measured undulator spectrum

The spectrum emitted by the cryogenic undulator U18 has been measured on the NANOSCOPIUM long beam line. Figure 21 shows the photon flux on the harmonics H9, H11, and H13 of the spectrum measured on the beam line and compared to the one calculated from the magnetic measurements using the parameters of Table II.

A very good agreement has been found in terms of bandwidth between the measured spectrum on the beam line and the calculated one from the magnetic measurements. This result confirms that the magnetic measurements carried out had high precision.

Figure 22 compares measured spectra with simulations for an ideal undulator, on the 9th and 10th harmonics [in Fig. 22(a)] and 13th and 14th [in Fig. 22(b)]. The intensity

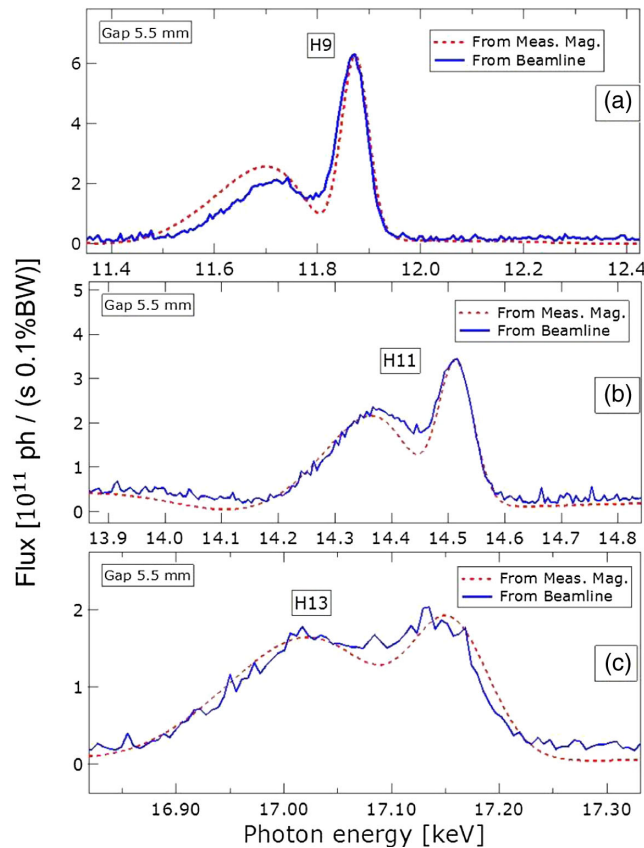


FIG. 21. Normalized spectra measured on the beam line (nonabsolute) and calculated from magnetic measurements at 5.5 mm gap through a 0.05 mm \times 0.05 mm aperture at a distance of 20.3 m from the undulator. Electron beam parameters of table II, with $\beta_x = 8.906$ m, $\beta_z = 7.216$ m, $\alpha_x = -1.296$ rad, $\alpha_z = -1.477$ rad. (a): 9th harmonic, (b): 11th, and (c): 13th harmonic.

has been normalized to H9 peak (from magnetic measurements). The respective intensities of H9 with respect to the H10 in the measurement and ideal case are in rather good agreement, so there are no particular undulator defects enhancing significantly the even harmonics. The slight discrepancy on the even harmonic could be due to the residual phase error, which appears to be very low. The intensity decay for the H13 and H14 with respect to the ideal case can be due to defects in the measurement calibration and of the undulator itself. Their respective intensities are indeed in rather good agreement. In all the cases, the measured and ideal harmonic line bandwidths are in good agreement, underlining the good quality of the undulator magnetic field.

2. Photon beam based alignment of the undulator

After the installation of an undulator in a storage ring, the magnetic axis is well aligned with the electron beam, to ensure the best performance possible. When the user beam line starts to be commissioned, the undulator alignment can

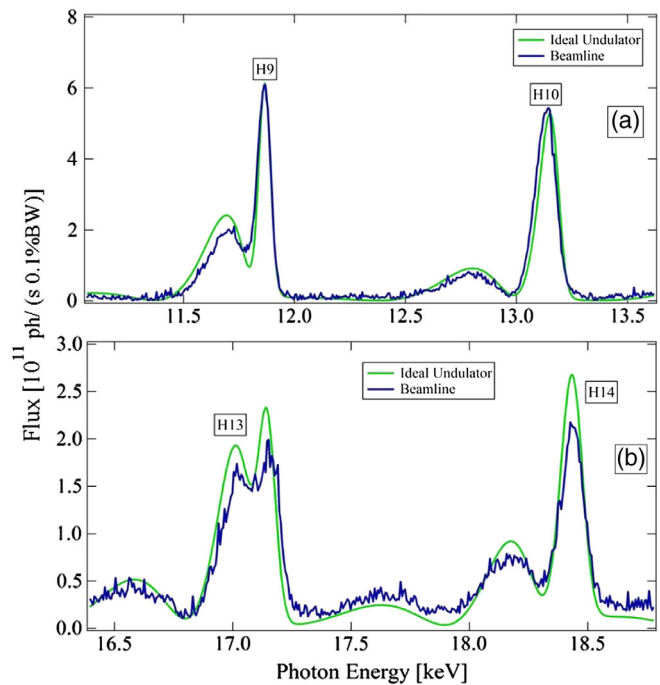


FIG. 22. (Green) spectra computed by an ideal undulator using SRWE with beam characteristics as Fig. 21. (Blue) spectra from the beam line normalized to H9 of ideal undulator.

be performed in a more precise manner in looking at the undulator harmonic shapes for different electron translation and angle bumps.

After some time, misalignment might occur and it is worth checking with the photon beam alignment. Thus experiments have been done on the spectrum of the undulator radiation with the NANOSCOPIUM beam line at SOLEIL, to ensure good alignment.

3. Offset optimization

One illustrates here an offset optimization while monitoring the spectrum of the undulator radiation on the NANOSCOPIUM long section beam line with a window aperture (0.2 mm \times 0.8 mm) placed 77 m away from the undulator, and a photodiode placed at a distance of 83 m. The adjustment has been done by monitoring the 11th harmonic, since high harmonics are very sensitive to any change in the beam parameters or the undulator characteristics. The offset was varied, as in moving the girders up or down, while keeping the magnetic gap constant (5.5 mm).

Figure 23 shows the spectra of the 11th as the offset is varied from -0.1 mm up to 0.4 mm. The slight variation of the resonant energy is caused by the decrease of the magnetic field due to the offset variation [see Eq. (1)].

Figure 24 shows the evolution of the intensity and bandwidth versus the offset variation. The best alignment is found when the highest intensity with the lowest half band width are observed. Therefore U18 offset had been

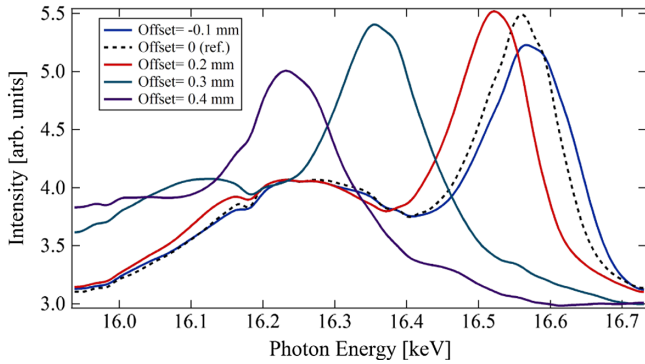


FIG. 23. Spectra measured (uncalibrated energy monochromator) on the NANOSCOPIUM beam line through a window aperture of 0.2 mm \times 0.8 mm placed at a distance of 77 m from the undulator with electron beam parameters shown in Table II, but with current $I = 17$ mA, $\beta_x = 7.507$ m, $\beta_z = 2.343$ m, $\alpha_x = -0.846$ rad, $\alpha_z = 0.03$ rad.

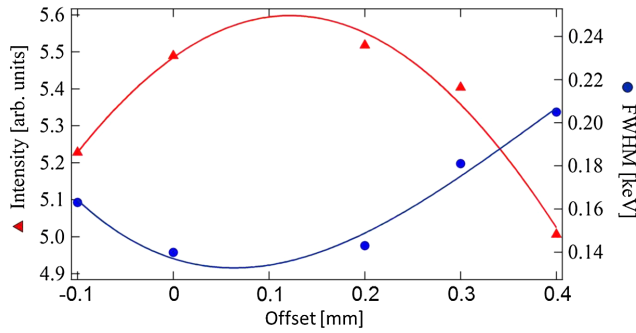


FIG. 24. Intensity and Full Width Half Maximum (FWHM) of the 11th harmonic as a function of the offset that varied from 0.3 mm up to 0.8 mm.

adjusted by 100 μ m to achieve the best alignment possible as in highest intensity.

These photon beam based alignment techniques are also carried out with electron (translation, angle) in the undulator, for a precise knowledge of the magnetic axis.

4. Taper optimization

Undulator tapering refers to variation of the deflection parameter (either changing the peak field or period length) along the undulator axis. Undulator tapering technique is vastly used for different purposes, such as compensation of the beam energy loss due to spontaneous undulator radiation, power increase of a high-gain FEL, energy scan with a more constant intensity concerning synchrotron radiation, etc.

Here, the experiment aimed to achieve the maximum peak intensity and minimum taper, i.e., to find the zero taper operation mode of the undulator. One way to modify the field is to slightly vary the gap at the exit of the undulator, either by closing or opening the girders at the

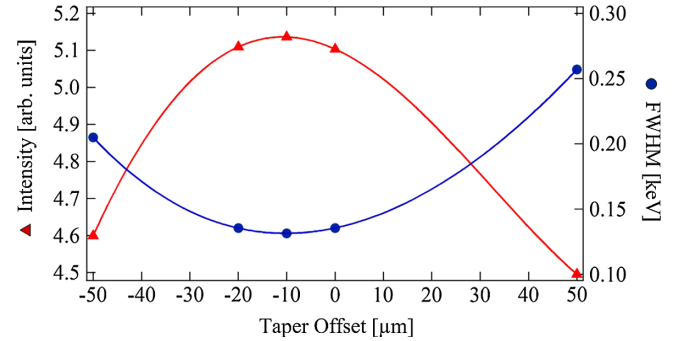


FIG. 25. Intensity and Full Width Half Maximum (FWHM) of the 11th harmonic as a function of the taper offset.

extremity. Figure 25 shows the change of intensity of the 11th harmonic as we change the taper value.

The highest intensity with the lowest band width is at -10 μ m; i.e., the girders at the end of the undulator are closed by 10 μ m. This optimization was useful for the beam line at a precision of ~ 5 μ rad corresponding to the angle of the internal girders, and increased the flux by $\sim 0.6\%$.

5. Five years of operation

The undulator has been installed in the storage ring since August 2011. The cryosystem, which is installed out of the tunnel, is connected to the undulator thanks to 2 flexible lines of 15 m each via a “valve panel.” This panel was developed by SOLEIL enabling to change the cryosystem while keeping the undulator at cryogenic temperature. This operation has been done only once in July 2014 where an ice plug blocked the flow in a line between the panel and the cryosystem. After some tests, it appeared that this ice plug was in the panel which was bypassed until the end of the run. During the tests and the bypass of the panel, the undulator started to warm-up leading to a beam loss of 4 hours due to a vacuum interlock. This failure was the only problem on this cryogenic device in 5 years which led to a beam loss. Parameters of the cryosystems have been adjusted with the beam so that the thermal longitudinal gradient remains below 3 K, while not decreasing the lifetime of the cryogenic pump. No disturbances have been observed on the beam due to the liquid flow, whatever the parameters used for the cryosystem. The undulator is warmed up one or twice a year, during electrical tests.

V. CONCLUSION

A 2 m $\text{Pr}_2\text{Fe}_{14}\text{B}$ cryogenic undulator with 18 mm period has been designed so that it suits for the NANOSCOPIUM long section beamline of SOLEIL. The use of $\text{Pr}_2\text{Fe}_{14}\text{B}$ permits us to operate at the liquid nitrogen temperature without undergoing SRT effects resulting in an increase of the magnetic field peak, and attain a good thermal stability along the undulator. In contrast, $\text{Nd}_2\text{Fe}_{14}\text{B}$ based CPMU requires thermal resistances distributed along the girders for

an operation at 140 K. The CPMU has been built, optimized at room temperature. It has been further corrected at cryogenic temperature using an additional in-vacuum measurement bench leading to a rms phase error of 3°.

After the installation at SOLEIL storage ring, it has been commissioned for different electron beam filling modes and different gaps. The thermal behavior of the undulator is stable because the maximum operation temperature variation for all electron beam filling modes and gap variations is less than 3 K. Effects on the electron beam are in agreement with the magnetic measurements.

The spectrum has been measured on the beam line and shows a very good agreement with the one calculated from the magnetic measurements. Photon beam based alignment for the NANOSCOPIUM beam line provides a very fine tuning of the undulator axis. The spectra are also very nice tools for the taper optimization allowing for a precision of 5 μ rad.

ACKNOWLEDGMENTS

We would like to thank Joel Chavanne from ESRF for his kind support, and members of the Accelerator and Engineering Division of SOLEIL led by A. Nadji. The authors are also very grateful for the support of J. M. Filhol, the former head of the Accelerator Division of SOLEIL and the European Research Council for the advance Grant No. COXINEL (340015).

-
- [1] M.-E. Couprie and J.-M. Filhol, X radiation sources based on accelerators, *C.R. Phys.* **9**, 487 (2008).
- [2] M. E. Couprie, New generation of light sources: Present and future, *J. Electron Spectrosc. Relat. Phenom.* **196**, 3 (2014).
- [3] P. Cloetens, R. Barrett, J. Baruchel, J.-P. Guigay, and M. Schlenker, Phase objects in synchrotron radiation hard x-ray imaging, *J. Phys. D* **29**, 133 (1996).
- [4] K. Gaffney and H. Chapman, Imaging atomic structure and dynamics with ultrafast x-ray scattering, *Science* **316**, 1444 (2007).
- [5] P. Elleaume, J. Chavanne, and B. Faatz, Design considerations for a 1 Å SASE undulator, *Nucl. Instrum. Methods Phys. Res., Sect. A* **455**, 503 (2000).
- [6] M. E. Couprie and M. Valléau, in *Proceedings of the 6th Int. School Synchrotron Radiation and Magnetism (Mittelwihr, France)* (Springer, Berlin, 2012), p. 51.
- [7] K. Halbach, Physical and optical properties of Rare Earth Cobalt magnets, *Nucl. Instrum. Methods Phys. Res.* **187**, 109 (1981).
- [8] K. Halbach, Permanent magnet undulators, *J. Phys. Colloques* **44**, C1-211 (1983).
- [9] W. Gudat, J. Pflüger, J. Chatzipetros, and W. Peatman, An undulator/multipole wiggler for the BESSY storage ring, *Nucl. Instrum. Methods Phys. Res., Sect. A* **246**, 50 (1986).
- [10] S. Yamamoto, T. Shioya, M. Hara, H. Kitamura, X. W. Zhang, T. Mochizuki, H. Sugiyama, and M. Ando, Construction of an in-vacuum type undulator for production of undulator x-rays in the 5–25 keV region, *Rev. Sci. Instrum.* **63**, 400 (1992).
- [11] F. H. O'Shea, G. Marcus, J. Rosenzweig, M. Scheer, J. Bahrndt, R. Weingartner, A. Gaupp, and F. Grüner, Short period, high field cryogenic undulator for extreme performance x-ray Free Electron Lasers, *Phys. Rev. ST Accel. Beams* **13**, 070702 (2010).
- [12] T. Bizen, Y. Asano, T. Hara, X. Marechal, T. Seike, T. Tanaka, H. Lee, D. Kim, C. Chung, and H. Kitamura, Baking effect for NdFeB magnets against demagnetization induced by high-energy electrons, *Nucl. Instrum. Methods Phys. Res., Sect. A* **515**, 850 (2003).
- [13] J. Chavanne, C. Penel, B. Plan, and F. Revol, In-vacuum undulators at ESRF, *Proceedings of the 2003 Particle Accelerator Conference, Portland, USA* (Institute of Electrical and Electronics Engineers (IEEE), New York, 2003), Vol. 1, pp. 253–255.
- [14] T. Hara, T. Tanaka, H. Kitamura, T. Bizen, X. Maréchal, and T. Seike, Insertion devices of next generation, in *APAC2004, Gyeongju, Korea* (JACoW, Geneva, 2004), p. 216.
- [15] H. Kitamura, Recent trends of insertion-device technology for x-ray sources, *J. Synchrotron Radiat.* **7**, 121 (2000).
- [16] D. Givord, H. Li, and R. P. de la Bâthie, Magnetic properties of Y₂Fe₁₄B and Nd₂Fe₁₄B single crystals, *Solid State Commun.* **51**, 857 (1984).
- [17] L. García, J. Chaboy, F. Bartolomé, and J. Goedkoop, Orbital Magnetic Moment Instability at the Spin Reorientation Transition of Nd₂Fe₁₄B, *Phys. Rev. Lett.* **85**, 429 (2000).
- [18] S. Hiroswawa, Y. Matsuura, H. Yamamoto, S. Fujimura, M. Sagawa, and H. Yamauchi, Magnetization and magnetic anisotropy of R₂Fe₁₄B measured on single crystals, *J. Appl. Phys.* **59**, 873 (1986).
- [19] H. Hiroyoshi, M. Yamada, N. Saito, H. Kato, Y. Nakagawa, S. Hiroswawa, and M. Sagawa, High-field magnetization and crystalline field of R₂Fe₁₄B and R₂Co₁₄B, *J. Magn. Mater.* **70**, 337 (1987).
- [20] D. Goll, M. Seeger, and H. Kronmüller, Magnetic and microstructural properties of nanocrystalline exchange coupled PrFeB permanent magnets, *J. Magn. Mater.* **199**, 49 (1998).
- [21] T. Hara, T. Tanaka, H. Kitamura, T. Bizen, X. Maréchal, T. Seike, T. Kohda, and Y. Matsuura, Cryogenic permanent magnet undulators, *Phys. Rev. ST Accel. Beams* **7**, 050702 (2004).
- [22] T. Tanaka, R. Tsuru, T. Nakajima, and H. Kitamura, Magnetic characterization for cryogenic permanent-magnet undulators: A first result, *J. Synchrotron Radiat.* **14**, 416 (2007).
- [23] T. Tanabe, J. Ablett, L. Berman, D. A. Harder, S. Hulbert, M. Lehecka, G. Rakowsky, J. Skaritka, A. Deyhim, E. Johnson *et al.*, X-25 cryo-ready in-vacuum undulator at the NSLS, *AIP Conf. Proc.* **879**, 283 (2007).
- [24] T. Tanabe, O. Chubar, D. A. Harder, M. Lehecka, J. Rank, G. Rakowsky, C. Spataro, R. Garrett, I. Gentle, K. Nugent *et al.*, Cryogenic field measurement of Pr₂Fe₁₄B undulator

- and performance enhancement options at the NSLS-II, *AIP Conf. Proc.* **1234**, 29 (2010).
- [25] C. Kitegi, P. Cappadoro, O. Chubar, T. Corwin, D. Harder, P. He, H. Fernandez, G. Rakowsky, C. Rhein, J. Rank *et al.*, Development of a PrFeB cryogenic undulator at NSLS-II, *Proceedings of IPAC2012, New Orleans, Louisiana, USA* (JACoW, Geneva, 2012), Vol. 12, p. 762.
- [26] J. Bahrtdt, H. Bäcker, M. Dirsatt, W. Frentrup, A. Gaupp, D. Just, D. Pflückhahn, M. Scheer, B. Schulz *et al.*, in *Proceedings of the International Particle Accelerator Conference, Kyoto, Japan* (ICR, Kyoto, 2010), p. 3111.
- [27] C. Benabderrahmane, P. Berteaud, M. Valléau, C. Kitegi, K. Tavakoli, N. Béchu, A. Mary, J. Filhol, and M. Couprie, Nd₂Fe₁₄B and Pr₂Fe₁₄B magnets characterisation and modelling for cryogenic permanent magnet undulator applications, *Nucl. Instrum. Methods Phys. Res., Sect. A* **669**, 1 (2012).
- [28] M. Couprie, C. Benabderrahmane, P. Berteaud, F. Briquez, C. Bourassin-Bouchet, F. Bouvet, L. Cassinari, L. Chapuis, M. Diop, J. Daillant *et al.*, in *Proceedings FEL, Basel, Switzerland* (JACoW, Geneva, 2014), Vol. 14.
- [29] C. Kitegi, J. Chavanne, D. Cognie, P. Elleaume, F. Revol, C. Penel, B. Plan, and M. Rossat, Development of a cryogenic permanent magnet in-vacuum undulator at the ESRF, *Proceedings of EPAC 2006, Edinburgh, Scotland* (JACoW, Geneva, 2006), Vol. 6, pp. 3559–3561.
- [30] J. Chavanne, M. Hahn, R. Kersevan, C. Kitegi, C. Penel, F. Revol, and E. G. France, in *Proceedings of the 11th European Particle Accelerator Conference, Genoa, 2008* (EPS-AG, Genoa, Italy, 2008), p. 2243.
- [31] C. Ostenfeld and M. Pedersen, in *Proceedings of the International Particle Accelerator Conference, Kyoto, Japan* (ICR, Kyoto, 2010), Vol. 10, p. 3093.
- [32] T. Tanaka, T. Seike, A. Kagamihata, H. Kitamura, T. Schmidt, A. Anghel, M. Brügger, W. Bulgheroni, and B. Jakob, *Proceedings of the International Particle Accelerator Conference, Kyoto, Japan* (ICR, Kyoto, 2010), Vol. 10, p. 3147.
- [33] J.-C. Huang, C.-H. Chang, C.-H. Chang, T.-Y. Chung, C.-S. Hwang, H. Kitamura, C.-K. Yang, and Y. T. Yu, in *7th International Particle Accelerator Conference (IPAC'16), Busan, Korea, May 8-13, 2016* (JACoW, Geneva, 2016), p. 1080.
- [34] O. Chubar, P. Elleaume, and J. Chavanne, A three-dimensional magnetostatics computer code for insertion devices, *J. Synchrotron Radiat.* **5**, 481 (1998).
- [35] J. Chavanne, P. Elleaume, and P. Van Vaerenbergh, End field structures for linear/helical insertion devices, *Proceedings of the 1999 Particle Accelerator Conference* (JACoW, Geneva, 1999), Vol. 4, p. 2665.
- [36] O. Chubar and P. Elleaume, Accurate and efficient computation of synchrotron radiation in the near field region, *Proceedings of the EPAC98 Conference*, (JACoW, Geneva, 1998), p. 1177.
- [37] R. Walker, Interference effects in undulator and wiggler radiation sources, *Nucl. Instrum. Methods Phys. Res., Sect. A* **335**, 328 (1993).
- [38] R. P. Walker, Phase errors and their effect on undulator radiation properties, *Phys. Rev. ST Accel. Beams* **16**, 010704 (2013).
- [39] J. Chavanne, C. Penel, and P. Van Vaerenbergh, Construction of Apple II and in vacuum undulators at ESRF, in *Proceedings of the 2001 Particle Accelerator Conference, Chicago* (JACoW, Geneva, 2001), Vol. 4, pp. 2459–2461.
- [40] O. Chubar, O. Rudenko, C. Benabderrahmane, O. Marcouille, J. Filhol, and M. Couprie, Application of genetic algorithms to sorting, swapping and shimming of the SOLEIL undulator magnets, *AIP Conference Proceedings* **879**, 359 (2007).
- [41] P. Elleaume and X. Marechal, Report No. ESRF-SR/ID-91-54, 1991.
- [42] T. Tanaka, T. Seike, A. Kagamihata, T. Schmidt, A. Anghel, M. Brügger, W. Bulgheroni, B. Jakob, and H. Kitamura, In situ correction of field errors induced by temperature gradient in cryogenic undulators, *Phys. Rev. ST Accel. Beams* **12**, 120702 (2009).
- [43] C. Kuhn, H.-J. Baecker, J. Bahrtdt, A. Gaupp, and B. Schulz, in *Proceedings of the 4th International Particle Accelerator Conference, IPAC-2013, Shanghai, China, 2013* (JACoW, Shanghai, China, 2013), p. 2126.
- [44] A. Loulergue, C. Benabderrahmane, F. Bouvet, P. Brunelle, M. Couprie, J. Denard, T. Moreno, A. Nadji, L. Nadolski, F. Polack *et al.*, in *Proceedings of the International Particle Accelerator Conference, Kyoto, Japan* (ICR, Kyoto, 2010), p. 2496.
- [45] A. Somogyi, C. M. Kewish, F. Polack, and T. Moreno, The scanning nanoprobe beamline nanoscopium at synchrotron soleil, *AIP Conf. Proc.* **1365**, 57 (2011).
- [46] A. Somogyi, K. Medjoubi, C. Kewish, V. Le Roux, M. Ribbens, G. Baranton, F. Polack, and J. Samama, Status of the nanoscopium scanning nanoprobe beamline of synchrotron SOLEIL, *SPIE Optical Engineering Applications*, 885104 (2013).